بسم الله الرحمن الرحيم

King Fahd university of Petroleum & Minerals

Deanship of Student Affairs

Vice Deanship for Student Excellence & Success

جامعة الملك فهد للبترول والمعادن

عمادة شؤون الطلاب

وكالة العمادة للتميز والنجاح

Undergraduate Research Office (URO)

Summer Undergraduate Research Experience - SURE223

Final Report

Student's name	Mohammed Alsadah	Research Interest (Summer training or research experience)	Summer training
ID	201913930	Research Topic	Effect of N_2/Ar Flow Rate Ratio on the Properties of Zinc Nitride Thin Films Grown by Magnetron Sputtering
Department	Physics		
Level	Junior		

Advisor

Name: Dr. Muhammed Baseer Haider (Associate Professor, Physics Department)

Research Center: Interdisciplinary Research Center for Renewable Energy and Power Systems (IRC-REPS)

Date: 8/27/2023

Student's Signature

Advisor's Signature

Contents

Effect of N2/Ar Flow Rate Ratio on the Properties of Zinc Nitride Thin Films Grown by Magnetron Sputtering

Mohammed Alsadah[1] and Muhammed Baseer Haider[2]

[1]King Fahad University For Petroleum and Minerals
[2]Interdisciplinary Research Center for Renewable Energy and Power Systems

October 22, 2023

Abstract

In this report, we investigate the optical and electrical properties of zinc nitride Zn_3N_2 thin films grown by DC magnetron sputtering. Films were prepared by sputtering zinc target in an ambient of nitrogen and argon gasses. During the deposition argon flow rate was kept constant whereas different nitrogen flow rates were used for each film. Structural, optical, and electronic properties of the films were studied using X-ray diffraction, UV-Vis-NIR spectrophotometry, and resistivity and hall effect measurements respectively. The lattice constant was obtained from XRD analysis. Thickness and bandgap of the films were calculated using the transmission spectra. Resistivity as well as carrier density and mobility were measured using Hall Effect. A correlation between structural, optical, and electronic properties and nitrogen to argon flow rate ratio was established.

1 Introduction

Zinc nitride (Zn_3N_2) is a semiconducting inorganic compound with an anti-bixbyite crystal structure [1]. Zinc nitride is a promising material in the semiconductors industry due to its low cost and abundance of its constituents. It has excellent electrical properties like low resistivity and high electrons density and mobility which makes it convenient to be used in electronics applications such thin film transistors (TFT) and photonics.

Zinc nitride was first successfully synthesized in 1940 in the form of powder [2]. Zinc nitride is a highly reactive compound that can react with gases and ambient atmosphere to form $ZnO/Zn(OH)_2$ medium. This means that Zn_3N_2 has a low stability which makes it a difficult material to synthesize. It was observed that thermal annealing can increase its stability [3]. This material can be synthesized in many ways [4] such as nitridation chemical reaction given by:

$$3Zn\,(s) + 2NH_3\,(g) \rightarrow Zn_3N_2\,(s) + 3H_2(g)$$

In which Zinc is heated to a temperature of 600°C and is exposed to ammonia gas. Other methods of fabricating thin films are chemical vapor deposition, molecular beam epitaxy and magnetron sputtering [5]. The bandgap of zinc nitride is not exactly established, and it depends on the method of synthesis [6]. Kazuaki et al found the direct bandgap to be 1.01eV [7], while Senadim et al [8] found it to be between 2.91eV - 3.24eV as direct bandgap and between 1.91eV - 3.06eV as indirect bandgap both after annealing.

2 Zinc nitride crystal structure

Zn_3N_2 has a body centered cubic (bcc) anti-bixbyite crystal structure. It has a conventional unit cell with 80 atoms [9]. Zn_3N_2 has a structure that resembles that of bixbyite mineral Mn_2O_3 except that ions have reversed roles and hence the name anti-bixbyite. To illustrate this, consider the crystal structure of bixbyite and anti-bixbyite shown in fig.1. In the anti-bixbyite structure Zn^{2+} is bonded to four N^{3-} ions forming a distorted trigonal pyramidal where Zn^{2+} is placed in the middle of the trigonal pyramidal. For nitrogen ions, there exist two sites (which will be detailed later), where N^{3-} is bonded to six Zn^{2+} forming two different distorted octahedrons. In the bixbyite case, anions $O^{2-}$are the ones bonded to four Mn^{3+} ions forming what resembles a seesaw shape, while Mn^{3+} cations are bonded to six O^{2-} anions in two different sites to form two different octahedrons.

Zinc nitride belongs to space group $Ia\bar{3}$ and has lattice constant of 9.78Å and a lattice volume for the conventional unit cell of 921.57 $Å^3$.

There are 3 Wyckoff positions in the structure. Two of which are occupied by nitrogen, and these are N1 and N2 sites and have 8b and 24d Wyckoff positions respectively, while Zn has 48e Wyckoff position. The crystal structure of zinc nitride is distorted which makes Zn-N2 have three different bond lengths. Bonds length between Zn and site N1 atoms is 2.14Å, and for Zn and N2 site atoms the bond lengths are 2.01Å, 2.06Å, 2.33Å [13]. The defects in lattice are due to vacancies and self-interstitials.

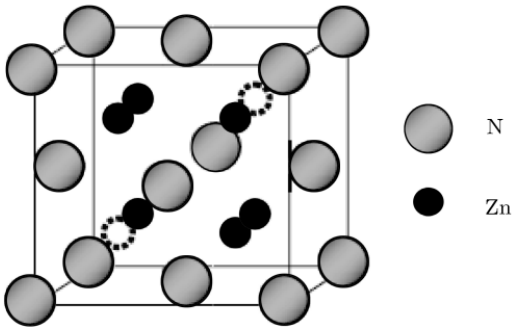

Figure 1: Crystal structure of Zinc nitride [8]

3 Thin Films Growth Methods

The growth of thin films is done mainly in two ways, physical vapor deposition and chemical vapor deposition.

3.1 Physical Vapor deposition

Depositing thin films requires (in principle) a target material from which atoms or molecules are removed and placed on a substrate. This can be furtherly subdivided into deposition using either evaporation or sputtering [11]. The method of evaporation was first done by the English physicist Michael Faraday in 1857 by using the method of exploding wire which enabled him to deposit gold thin films. This evaporation method was preceded by sputtering which was discovered by Grove in 1852 [12].

3.1.1 Thermal evaporation

Deposition by evaporation can be done in different ways. One way is through *thermal evaporation* which is a method in which a metal is used as a source of evaporation and is placed in an evaporator called the *evaporation boat*, which is made of metals like tungsten, molybdenum, or tantalum due to their high melting points. The boat is connected to a power supply that provides a DC current of several hundred amps. The

boat undergoes the so-called *Joule heating* or *resistive heating* maintaining the boat at high temperature and making it glow. This makes the metal melt and then evaporate moving unimpeded to the substrate and depositing on it.

3.1.2 Electron beam evaporation

Alternative way of evaporation is electron beam evaporation. This method uses electron gun to hit the source material that we want to evaporate and heats it up until it vaporizes or sublimes. This electron gun is made of tungsten filament that is heated by running an electrical current through it until it glows. This filament is shielded from the substrate so that no contamination occurs. The filament then gets thermally excited and has thermionic emissions. The emitted electrons are then steered to the target by using magnetic field. The sample in this method is placed in a crucible made of copper, tungsten or ceramic which is cooled using water circulation. Electron beam evaporation technique has the advantage of being able to deposit more than one material simultaneously. In addition, this method offers purity for the films more than that in thermal evaporation and also since the crucible is cooled and only the material is heated this allows for deposition of almost all metals even those with high evaporation points.

3.1.3 Sputtering

The last method we discuss in Physical vapor deposition is the sputtering process. This method, as in the case of evaporation, has many variants which are most of the time combined in one sputtering system [11]. Sputtering differs from evaporation techniques in that the target is not heated, rather it is bombarded with energized atoms making the target eject atoms and falls on the substrate (assuming that the substrate is below the target since some systems have it above the target). In sputtering deposition, the vacuum chamber is evacuated by vacuum pumps up to less than torr, then argon (Ar) gas is leaked in the chamber. This is due to its inertness and cheapness [13] which makes it effective in sputtering. Then, a voltage is applied between the cathode (near the target) and the anode (near the substrate) which in turn ionizes the argon and results in glow discharge plasma. The glow discharge occurs because the voltage is increased to some point called the breakdown voltage after which an insulator, in this case argon gas, becomes conductor. The strong electric field between the electrodes ionizes few atoms and these stripped electrons ionizes other atoms in a phenomenon called *Townsend Avalanche effect* or electron multiplication. The ionized positive argon atoms are now accelerated toward the cathode until they hit the target and sputter (eject) atoms from the target. Not only atoms are ejected from the targe, but we also have secondary electrons (electrons that are liberated from the atoms upon collisions) that are attracted to the anode and may in there way ionize other argon atoms making the glow discharge self-sustaining. The efficiency of the sputtering process is quantified by a quantity called the *sputter yield* which is defined as the number of atoms sputtered or removed from the target per colliding ion.

Variations of the method of sputtering exist such as DC sputtering, RF sputtering, magnetron sputtering, and reactive sputtering and usually sputtering systems have combination of these. We address each one briefly.

DC sputtering is the most basic sputtering method. In it, a DC voltage is applied between the target and the substrate. It is used mostly with conductive metals, and it has a high deposition rate. It cannot be used to deposit dielectric materials because of positive charge accumulation on the target which expels the positive ions.

RF sputtering operates on AC voltage with frequency of 13.56MHz which is a frequency designated for industrial, scientific, and medical applications so as not to interfere with radio communication waves. The RF sputtering process prevents charge build up and hence ideal for depositing insulators as well as conductors [14]. This comes at the cost of lower sputtering yield than that of DC sputtering.

Magnetron sputtering is when we couple a magnetic field with electric field coming from the DC or AC (in RF sputtering) power supply. Its function is to confine or localize electrons near the target so that it ionizes

more atoms leading to an increase in the sputtering yield. Moreover, this localization of electrons can lead to a uniform sputtering.

The last of these variations of the sputtering operation is the reactive sputtering. This can be coupled also with the DC and RF sputtering deposition. Reactive sputtering happens when we allow a reactive gas agent to enter the vacuum chamber and react midway with the ejected target atoms. Two gases are mostly used, and these are nitrogen N_2 and oxygen O_2 which enables the fabrication of metal nitrides and oxides.

4 Characterization methods

When we characterize thin films after depositing them, we mean that we want to study their properties like crystal structure or electronic structure or other optical properties like transmittance and reflectance, with that being said, there are different methods to accomplish that. We discuss some of these methods.

4.1 X-ray diffraction (XRD)

XRD is a technique used to determine the crystal structure of the studied material and also to calculate the lattice parameters or constants in such structure. X-ray diffraction was discovered by Max Von Laue while working with two of his colleagues Friedrich and Knipping in 1912 [15] using zinc sulfide for which Laue later on got the 1914 Nobel prize. The idea of X-ray diffraction was developed further by son and father collaboration, Lawrence Bragg, and henry Bragg. Lawrence explained the diffraction pattern obtained by Laue by thinking of crystals as atoms arranged on planes repeatedly throughout the material and that incident X-ray reflects and interferes with itself giving the diffraction pattern. From this idea, he formulated the famous Bragg's law:

$$n\lambda = 2d\sin\theta \tag{1}$$

Where n is the diffraction order and λ is the X-ray wavelength and d is the spacing between planes, while θ is the angle made between the plane of incidence and the incident beam. He went on then to share the 1915 Nobel prize, along with his father who designed the X-ray spectrometer.

The device used to do XRD is called diffractometer. The mechanism by which a diffractometer works is that an X-ray beam is generated by an X-ray tube and directed toward the sample. The beam diffracts in all directions so that a detector is used to collect radiation. The detector goes from a minimum angle to a maximum angle while collecting radiation. A graph is then generated showing the intensity of radiation versus 2θ which is the angle made between the reflected beam and the beam that experiences no reflection. From this graph, the peaks are indexed with the so-called miller indices and X-ray pattern is matched to existing ones to deduce these indices. From this, we can calculate the lattice constants, which we will do later in this report.

4.2 Spectrophotometry

This method is used to determine different optical constants like the refractive index and the optical bandgap and also the thickness of the films. The method uses ultraviolet light, visible light, and sometimes near infrared light to measure the transmittance or reflectance or absorbance of the material that is being studied. When only ultraviolet and visible light is used, we call it a UV-Vis spectrophotometer and when *near infrared* light is included, we call it UV-Vis-NIR spectrophotometer.

The working mechanism by which a spectrophotometer operates is the following: light is emitted from one or two sources to account for the different wavelengths. A single xenon lamp can be used to emit both UV and visible light but could be expensive [16]. An alternative is to use tungsten lamp to emit visible and NIR light while a deuterium lamp is used to account for UV. Then, light passes through a *monochromator* such as diffraction grating or prism to separate and select which wavelength passes. Light then goes through a

narrow slit and hits the sample (which could be a thin film, or a liquid poured in cuvette). The sample can either reflect, absorb, or transmit the light incident upon it. The transmitted beam is detected using a *photometer* which converts the intensity of the photons into an electric current which is then processed and read as the transmittance.

The data obtained is the transmittance versus the wavelength of the emitted light. The data can be plotted and analyzed to yield constants like the bandgap and refractive index and thickness of the films.

4.3 Resistivity and hall effect measurement

To determine electrical properties like resistivity and charge carrier density and carrier mobility we can use different methods such as the four-point contact method and Van Der Pauw (VDP) method. Since we determined these properties for zinc nitride using the later method, which can be referred to in the results and discussion section, we will spend this section talking about VDP method.

In VDP method, the thin film, which could be arbitrary in shape, is connected to four electrical probes that are placed on the perimeter of the sample. This configuration is shown in fig.2. To determine the resistivity of the film, two measurements must be made. The first is to run a current through contacts, say 1 and 2 resulting in I_{12} , at the same time we measure the voltage across the opposite contacts 3 and 4 to get V_{34} . The second measurement should be done for contacts perpendicular to the ones made in the first measurement, in our case I_{14} and V_{23} . Now we calculate the following resistances $R_{12,34} = \frac{V_{34}}{I_{12}}$ and $R_{14,23} = \frac{V_{23}}{I_{14}}$. From this we can use the equation derived by Van Der Pauw [17] to get the resistivity:

$$e^{-\frac{\pi R_{12,34} d}{\rho}} + e^{-\frac{\pi R_{14,23} d}{\rho}} = 1 \tag{2}$$

Where d and ρ are the thickness and resistivity of the thin film respectively. Sometimes the resistivity is expressed in sheet resistance R_s (measured in ohm/sqr) and is related to ρ by $\rho = R_s d$.

Measuring the carrier concentration or density is done by implementing the Hall effect. In this effect, an applied current is exposed to perpendicular magnetic field which steers the charge carriers to one side of the film according to the Lorentz force $\vec{F} = q\vec{v} \times \vec{B}$ where q , $\vec{v}$ and $\vec{B}$ and are the charge and velocity of the charge and the magnetic field respectively. Carriers being in one side of the film makes the other side charges up with the opposite sign. This creates a voltage V_H between the sides of the films called the hall voltage, which generates an electric field $E = \frac{V_H}{w}$ (where w is the width of the film) that has a force $\vec{F} = q\vec{E}$ that balances the force coming from the Lorentz force [18]. With the help of the equation for the drift velocity $v_d = \frac{I}{nqA}$ (where I is the current and n is the carrier density and A is the area of the film) and equating the two forces we can get $n = \frac{IB}{qV_H d}$ where d is the thickness of the film, which can also be written as $n_s = \frac{IB}{qV_H}$ where n_s is the sheet density that the device can measure. To get the hall voltage, two measurements should be made each with opposite magnetic field direction but same magnitude. In the first measurement, the voltage is taken diagonally, and the current is applied to the other diagonal and then we should reverse the process. The same is done in the second measurement but the direction of the magnetic field is reversed. This now enables us to calculate the Hall voltage and figure out the sheet density. In addition, we can use the resistivity and charge density to calculate the electron mobility.

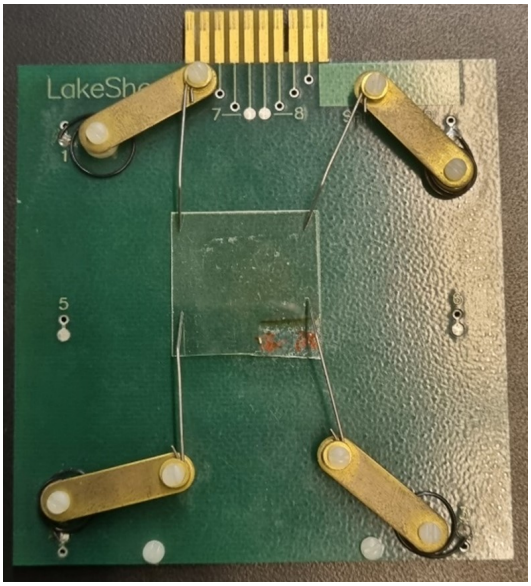

Figure 2: sample is connected to four electrical probes. The probes are numbered counterclockwise starting from the upper left.

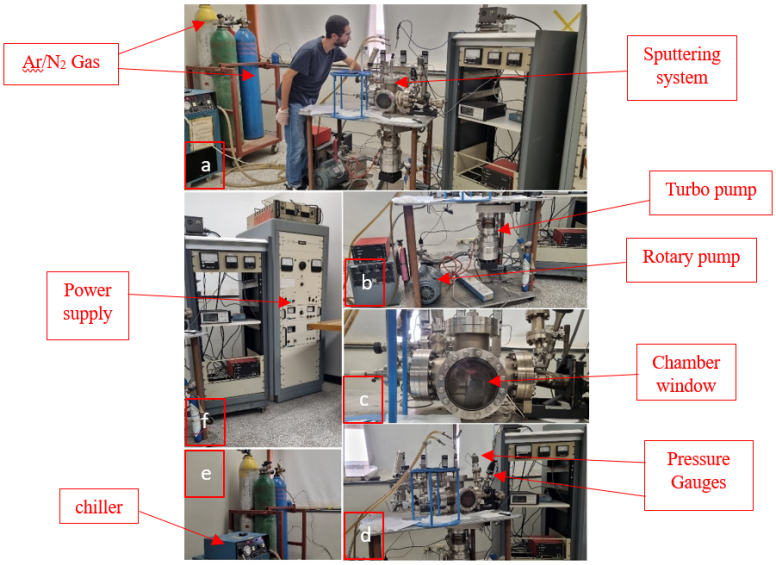

Figure 3: Starting from top and moving clockwise. a) a picture of the entire setup. b) three vacuum pumps with two mechanical pumps on the left and a turbomolecular pump on the right. c) sputtering chamber with dim plasma appearing on the window. d) sputtering system and pressure gauges. e) water coolant and gas cylinders. f) power supply on the right of pressure gauges.

5 Experimental

The setup and the sputtering system we are using, are as shown in Fig.3a. We placed the substrate inside the chamber and installed the target on the magnetron, which is located behind the chamber's window in

Fig.3c where the two steel surfaces are sealed. After the substrate and target are placed and the system is sealed, we start the vacuum pump to evacuate the system. There are three vacuum pumps, in our system, two of which are rotary pumps that can evacuate the system up to 10^{-2} torr. Then, the turbomolecular pump is turned ON to bring the chamber pressure to 10^{-5} - 10^{-6} torr. The chamber pressure is monitored using the pressure gauges controllers shown in Fig.3d on the right. The gauge controller on the middle shelf, *Inficon,* is used to measure pressure in the range 10^{-2} - 10^{-4} torr, under this range, the other gauge *Varian* is used. In Fig.3e, the water chiller and the gas cylinders are shown. The water chiller is used to keep the magnetron cool during its operation whereas gasses are used for the sputtering process [19]. The flow rate of gasses in the chamber are controlled by the leak valves and measured by the flow meters as shown in Fig.3a located behind the sputtering chamber. In our experiments, we used three different nitrogen gas flow rates namely 4.0mL/min, 1mL/min, and 8.8mL/min. After the water chiller is turned on and the gases are leaked into the chamber, DC power supply which is connected to the magnetron is turned on. A pink color plasma glows in the chamber and sputtering starts as can be seen in Fig.3c (it appears dim because the lab lights are ON). Sputtering was performed for a duration of 15 minutes. After the growth, the chamber is vented (the system is returned to atmospheric pressure) so that we can open the chamber and collect our deposited thin films. The chamber can be opened by lifting the top steel flange where the target is installed. This completes the sputtering deposition process.

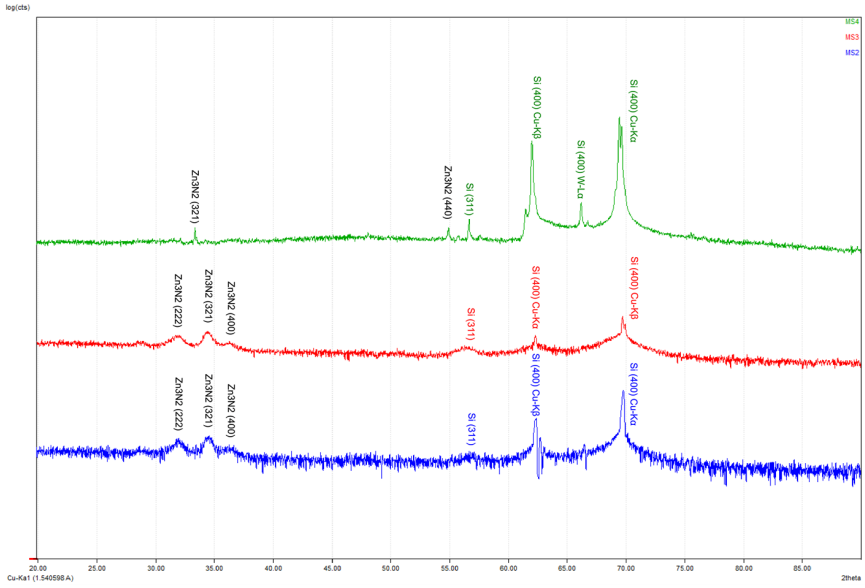

Figure 4: X-ray diffraction of all samples with miller indices above each peak. The peaks due to zinc nitride are written in black while those coming from silicon are written with same color of the respective plot.

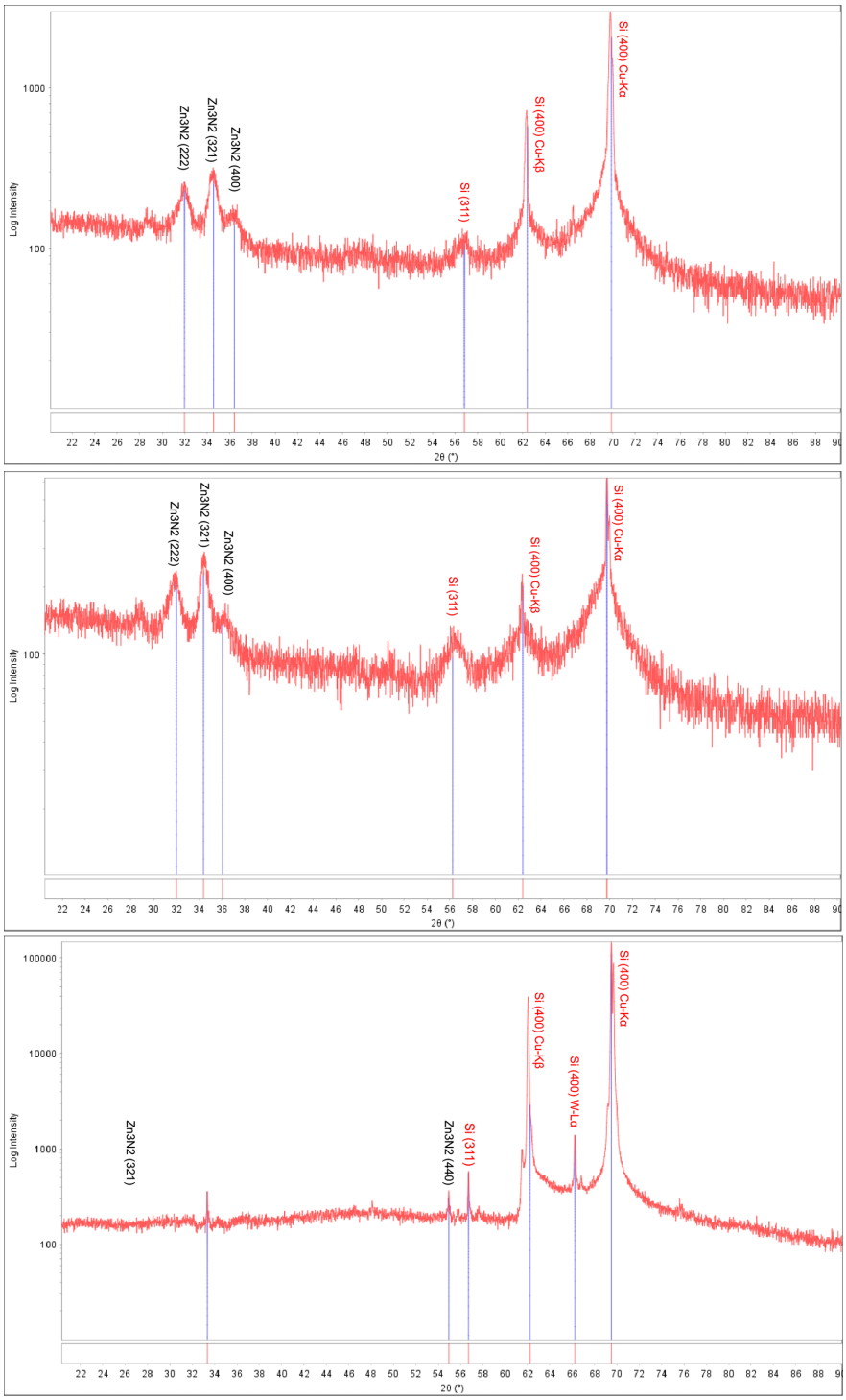

Figure 5: X-ray diffraction of each sample. From top to bottom a) MS2 b) MS3 C) MS4. Peaks coming from zinc nitride are indexed with black color while those from silicon (100) are indexed with red.

6 Results and discussion

We prepared three zinc nitride samples coated on silicon (100) and glass substrates simultaneously. Different nitrogen gas flow rates were used for each film during the deposition process. The samples were labelled as MS2, MS3, and MS4 corresponding to nitrogen flow rate of 4mL/min, 1mL/min, 8.8mL/min respectively, where each sample contained two films, one is deposited on Si (100) and the other on the glass substrate. The three samples are shown in Fig.6.

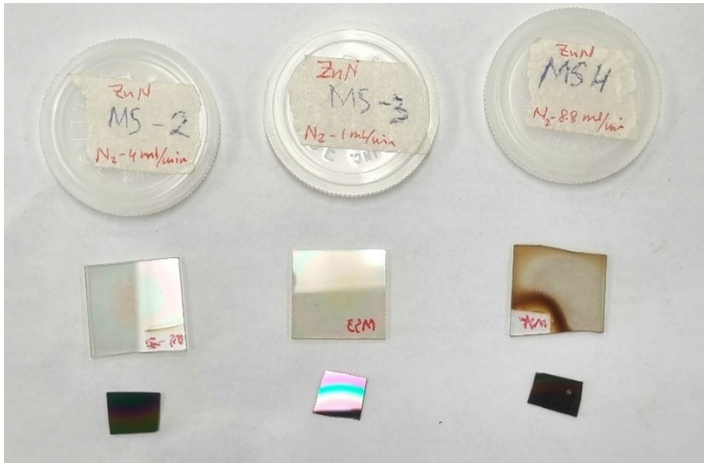

Figure 6: prepared samples using DC magnetron sputtering. Each sample contains zinc nitride deposited on glass substrate (middle) and silicone (100) substrate (bottom). The red writing on the glass substrate is used as a reference.

6.1 X-ray Diffraction

X-ray diffraction was performed on the films grown on Si(100) to study the crystallinity of the films. The X-ray diffractometer used is *LabX XRD-6000* made by *SHIMADZU*. The monochromatic X-ray source used in the diffractometer is CuK_α with wavelength of 1.54Å. The X-ray pattern obtained for the three films are shown in Fig.3, and Fig.4. The three diffraction peaks related to Zn_3N_2 with miller indices (222), (321), and (400) in samples MS2 and MS3, match with the Zn_3N_2 peaks obtained in references [5] and [7]. This confirms that zinc nitride has a body centered cubic (bcc) structure from which we were able to calculate the lattice constant. The peaks at $2\theta \approx 62°, 66°, 69°$ correspond to Si(400) CuK_β, Si(400) WL_α, and Si(400) CuK_α respectively[20].

A list of the peaks and their corresponding peak position (2θ) are shown in the table1. Peaks are numbered from left to right in the plots.

Peak No.	Peaks	MS2	MS3	MS4
1	Zn3N2(222)	31.98	32.01	-
2	Zn3N2(321)	34.56	34.38	33.36
3	Zn3N2(400)	36.35	36.27	-
4	Zn3N2(440)	-	-	54.95
5	Si(311)	56.83	56.26	56.71
6	Si(400) due to Cu(kb)	62.42	62.38	62.07
7	Si(400) due to W(La)	-	-	66.25
8	Si(400) due to Cu(ka)	69.88	69.77	69.5

Table 1: Each peak and its occurrence place. Note that angles are in degrees.

The lattice constant is calculated using Bragg's law $n\lambda = 2d\sin\theta$ along with the formula for interplanar distance for cubic lattice $d = \frac{a}{\sqrt{h^2+k^2+l^2}}$ where n is the diffraction order, λ is the wavelength of the incident radiation, and θ is the angle made by the incident beam and the plane of incidence. a refers to the lattice constant and h, k, and l are the miller indices. Using $n = 1$, the formula for the lattice constant is:

$$a = \frac{\lambda\sqrt{h^2 + k^2 + l^2}}{2\sin\theta} \tag{3}$$

Index	a (MS2) Å	a (MS3) Å	a (MS4) Å
Zn3N2(222)	9.68	9.67	-
Zn3N2 (321)	9.7	9.75	10.04
Zn3N2 (400)	9.87	9.9	-
Zn3N2 (440)	-	-	9.44
Average (Å)	9.75	9.77	9.74

Table 2: Lattice constant of Zn_3N_2 for different samples

So, the average lattice constant of our Zn_3N_2 thin films is which is close to that obtained in references [5],[8], and [9].

The full width at half maximum (FWHM) for the most prominent peak (321) are given in table 3.

FWHM (321)	Sample No.
1.41	MS2
1.27	MS3
0.36	MS4

Table 3: Full width at half maximum for Zn_3N_2 (321) peak for each sample.

6.2 UV-Vis-NIR spectrophotometry

Optical properties of the films were studied using UV-Vis-NIR spectrophotometry. We used this method to determine the refractive index, bandgap and the thickness of the films.

In spectrophotometry, the transmittance is plotted as a function of wavelength as shown in Fig.7a. Fringes in the transmittance spectra are due to interference of the beams reflected from the surface of the film and from the film-substrate interface. In the transmittance spectra, where the transmission suddenly drops to

almost zero percent is indicative of complete absorption of the incident beam by the sample. The thickness of the films can be calculated from the transmittance spectra using the following formula [21]:

$$d = \frac{\lambda_1 \lambda_2}{2\left|\lambda_1 n_2 - \lambda_2 n_1\right|} \tag{4}$$

Where λ_1 and λ_2 are either two consecutive maxima or two consecutive minima in the transmission spectrum. $n_1$and n_2 are the corresponding refractive indices for the given wavelengths. To calculate the refractive index of the films we used a method established by Swanepoel [21][22]. The crux of this method is to construct an upper and lower envelope in the region of fringes (A region of wavelength greater than 400nm in fig.7a).

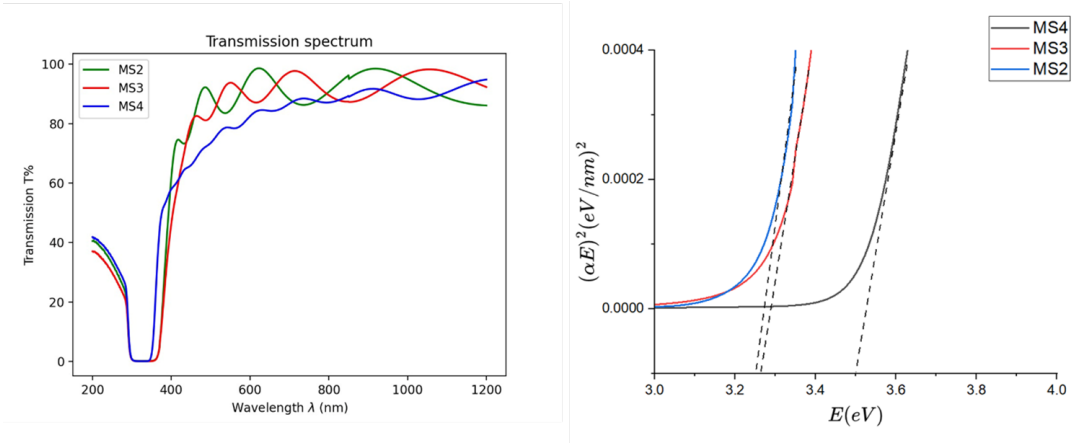

Figure 7: results of the transmission spectroscopy. a) transmission in percentage versus wavelength in nanometer. b) TAUC plot for $(\alpha E)^2$ in $\left(\frac{eV}{nm}\right)^2$ versus E in eV. The x-intercept represents the bandgap energy.

the upper and lower envelope are named $T_M(\lambda)$ and $T_m(\lambda)$ respectively and both of them are functions of the wavelength. Three equations are necessary to calculate the refractive index:

$$s = \frac{1}{T_s} + \left(\frac{1}{T_s^2} - 1\right)^{\frac{1}{2}} \tag{5}$$

$$N = 2s\frac{T_M - T_m}{T_M T_m} + \frac{s^2 + 1}{2} \tag{6}$$

$$n = \left[N + \left(N^2 - s^2\right)^{\frac{1}{2}}\right]^{\frac{1}{2}} \tag{7}$$

Where s in (5) is the refractive index of the substrate which is usually glass even in our measurement. We assumed that the refractive index for glass does not change very much and so we used $s = 1.52$ but the most accurate way is to calculate s as a function of the transmission for glass. In (6) N is taken to be a parameter. The result of the calculations are shown in Fig.8.

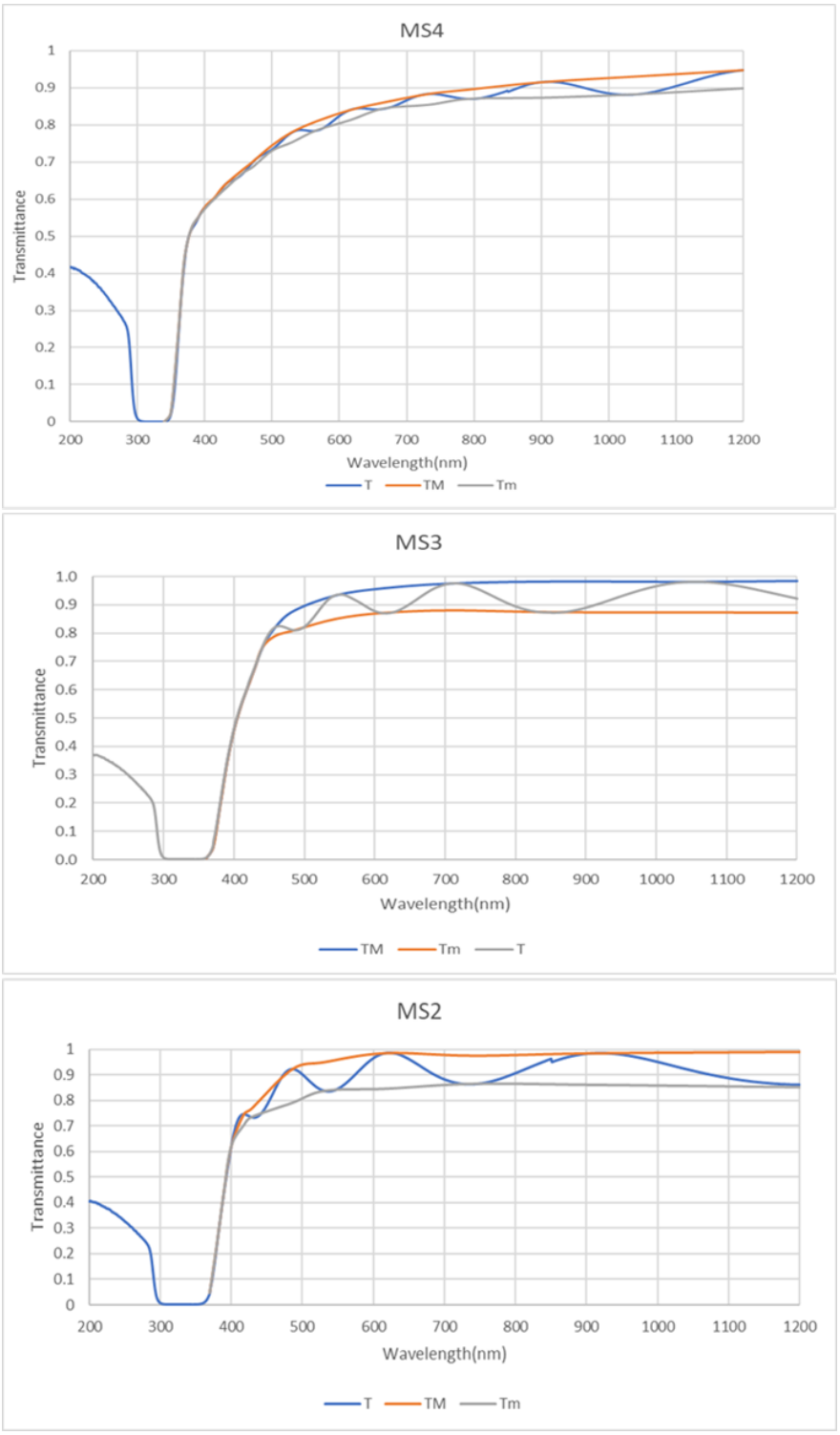

Figure 8: Envelope method applied to the transmittance spectra for each sample. TM and Tm are the upper and lower envelope respectively.

From the calculations of the refractive indices for the three samples and using equation (4) we were able to calculate the thickness for all samples.

Type	$\lambda_1(nm)$	$\lambda_2(nm)$	n_1	n_2	d(nm)
maxima	418	486	1.75	1.95	**2960.2**
maxima	486	618	1.95	1.93	556.82
maxima	618	914	1.93	1.89	473.49
minima	429	532	1.7	1.88	**1176.9**
minima	532	741	1.88	1.86	488.58
Average thickness	-	-	-	-	506.3

Table 4: Thickness calculations for MS2. Type refers to the wavelengths being either peaks or valleys.

Type	$\lambda_1(nm)$	$\lambda_2(nm)$	n_1	n_2	d(nm)
maxima	458	544	1.66	1.8	**1553.8**
maxima	544	707	1.8	1.81	671.31
maxima	707	1050	1.81	1.85	619.54
minima	485	611	1.78	1.8	682.33
minima	611	849	1.8	1.84	647.68
Average thickness	-	-	-	-	655.22

Table 5: Thickness calculations for MS3.

Type	$\lambda_1(nm)$	$\lambda_2(nm)$	n_1	n_2	d(nm)
maxima	530	617	1.66	1.64	1061.5
maxima	617	733	1.64	1.64	1172.7
maxima	733	903	1.64	1.68	1313.4
minima	566	666	1.64	1.6	994.09
minima	666	794	1.6	1.62	1428.6
minima	794	1040	1.62	1.69	1199.1
Average thickness	-	-	-	-	1194.9

Table 6: Thickness calculations for MS4.

So, for the three samples MS2 and MS3 and MS4, the thicknesses of the films are 506.30nm, 655.22, and 1194.9nm respectively. The calculated thicknesses that are marked bold in the tables indicate a huge difference from other data points. Thus, these thicknesses were excluded from the average calculation. This huge discrepancy is attributed to computation of the thickness using maxima or minima near the wavelength where the material starts absorbing, that is near 400-500nm range. As stated in Swanepoel's paper [21], equation (4) is not accurate and also sensitive to errors in the refractive index. To avoid such problems, it is better to discard the values obtained from the absorption range.

After calculating the thicknesses of the films, we can use the following relations to get the bandgap energy:

$$\alpha = \frac{1}{d} \ln \frac{1}{T} \tag{8}$$

$$\alpha E = \alpha_0 \left(E - E_0\right)^{\frac{1}{2}} \tag{9}$$

where α is the absorption and α_0 is a constant of proportionality and E is the energy, while E_0 is the bandgap energy. T should be calculated in decimals not in percentage.

If we squared equation (9) and then plotted $(\alpha E)^2$ versus E we get the so called TAUC plot which is shown in fig.7b. By using the linear portion of the graph and extrapolating it to the x-axis we can determine the bandgap of the film. The points where the lines touch the x-axis are shown in table 7.

Sample	Bandgap (eV)
MS2	3.25
MS3	3.26
MS4	3.5

Table 7: Each sample with its own bandgap

Since we obtained the thicknesses of the films and their corresponding bandgaps, this completes our spectrophotometry analysis.

6.3 Resistivity and hall effect measurements

The third characterization of thin films was done using Van der Pauw method (explained in *characterization methods* section) to measure the resistivity and charge carrier density and electron mobility. The system that was implemented to do the measurement is shown in Fig.9. The recorded measurements are displayed in the tables below. Note that the magnetic field was varied from -5kG to 0 and from 0 to 5kG.

B (kG)	I(A)	V
1	9.83	4
2	19.5	9.1
3	29.5	13.8
4	40.3	18.9
5	53.5	25.3

Table 8: The magnetic field and the corresponding current and voltage supplied.

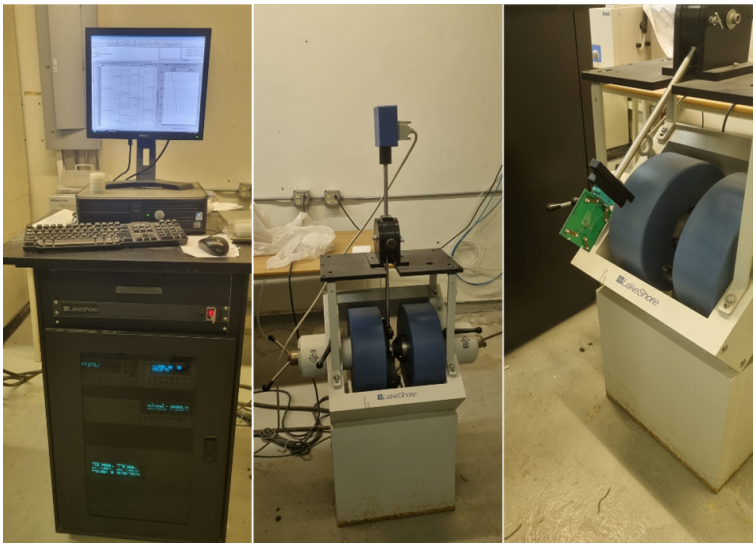

Figure 9: the setup used to do the measurements. From left to right a) the computer is used to configure the conditions for the experiment while the devices inside the cabinet are magnetometer (top shelf) and power supply, voltmeter, and ammeter (bottom shelf). b) device used to do the hall effect measurement. c) the sample is mounted on a circuit board using VDP method and placed between a magnetic field.

Field (G)	Sheet Resistivity (ohm/sqr)	Sheet Carrier Density ($1/cm^2$)	Hall Mobility ($cm^2/V{\cdot}s$)
-5000	11700	-4.88E+12	-101
-4000	12700	-4.39E+12	-113
-3000	12800	-2.57E+12	-193
-2000	12900	-1.92E+12	-258
-1000	12800	-8.74E+11	-566
0.01	13000	-	-
Average	12700	-2.93E+12	-246

Table 9: Electrical properties of MS2.

Field (G)	Sheet Resistivity (ohm/sqr)	Sheet Carrier Density ($1/cm^2$)	Hall Mobility ($cm^2/V{\cdot}s$)
0.02	10900	-	-
1000	11000	-4.37E+12	-160
2000	11000	-1.02E+12	-684
3000	11000	-8.75E+11	-799
4000	11100	-2.23E+12	-313
5000	11200	-3.95E+12	-177
Average	11000	-2.49E+12	-426

Table 10: Electrical properties of MS3

Field (G)	Sheet Resistivity (ohm/sqr)	Sheet Carrier Density (1/cm^2)	Hall Mobility (cm^2/V·s)
-5000	2270	-6.73E+11	-2920
-4000	3130	-4.60E+11	-4280
-3000	2330	-3.45E+11	-5710
-2000	2910	-2.27E+11	-8670
-1000	2650	-1.19E+11	-16500
0.01	2430	-	-
Average	2620	-3.65E+11	-7620

Table 11: Electrical properties of MS4

To get the bulk resistivity, we should multiply the sheet resistivity by the film thickness. Moreover, to get the carrier density we should divide the sheet carrier density by the film thickness.

Sample	Bulk resistivity (ohm-cm)	Carrier density (1/cm3)	Hall mobility (cm^2/V·s)
MS2	0.64	-5.78E+16	-246
MS3	0.72	-3.80E+16	-426
MS4	0.31	-3.05E+15	-7620

Table 12: Summary of the values measured by hall effect and VDP method

6.4 Relations

Before ending the *results and discussion* section, we want to investigate some relations, namely that of FWHM, charge density, and the bandgap against the flow rate by which the samples were deposited. The plots are depicted in Fig.10. For Fig.10a and Fig.10b we see that FWHM, and charge density decrease (but not strictly) with increasing flow rate while in Fig.10c the bandgap increases with increasing flow rate. Note that we plotted the charge density in magnitude only because the negative sign indicates the type of carriers, namely electrons.

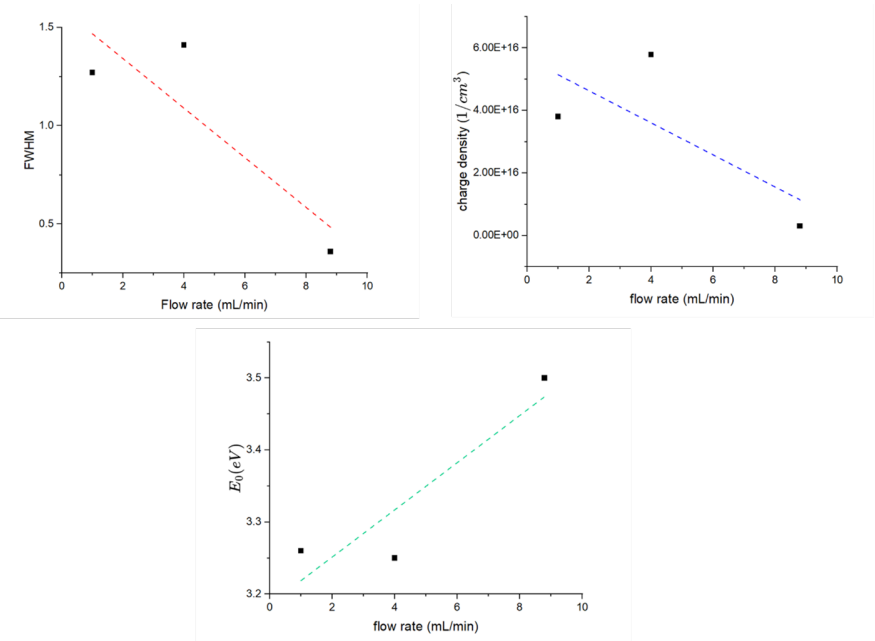

Figure 10: some thin films variables plotted against the flow rate of the samples. Upper left a) FWHM versus flow rate. b) charge density versus flow rate located upper right. Bottom c) bandgap versus flow rate.

7 Conclusion

In this article, we were successfully able to grow zinc nitride thin films using DC magnetron sputtering with different gas flow rates namely 4mL/min, 1mL/min, 8.8mL/min with 15min as the sputtering time. The films were characterized by XRD, and the resulting spectra were indexed. From the indexed patterns we calculated the lattice constant for samples MS2, MS3, and MS4 and we got 9.75Å, 9.77Å, and 9.74Å for each one respectively. We also computed FWHM for (321) peak, which revealed that MS4 has the sharpest peak being the one with minimum FWHM. The thickness was calculated from the transmission spectra with 506.30nm, 655.22nm, 1194.9nm corresponding to samples 2, 3, and 4. Using the thicknesses along with the equation of absorption and bandgap, we plotted the TAUC plot and extrapolated the bandgaps. The bandgaps computed are 3.25eV, 3.26eV, and 3.5eV. Resistivity and hall effect measurements were taken for which the results are displayed in *table 12*. Finally, we explored some relations between the gas flow rate and FWHM and carriers' density which when fitted showed a decrease with increasing flow rate while that for the bandgap was increasing.

References

1. Redondo-Cubero, A., Gómez-Castaño, M., Núñez, C. G., Domínguez, M., Vázquez, L., & Pau, J. L. (2017). Zinc nitride thin films: basic properties and applications. *Oxide-based Materials and Devices VIII*, *10105*, 209-214.

2. Juza, R., & Hahn, H. (1940). Uber die kristallstrukturen von Zn3N2, Cd3N2 und Ge3N4. metallamide und metallnitride. IX. mitteilung. Zeitschrift fur anorganische und allgemeine Chemie, 244(2), 125-132.

3. Trapalis, A., Farrer, I., Kennedy, K., Kean, A., Sharman, J., & Heffernan, J. (2020). Improved ambient stability of thermally annealed zinc nitride thin films. *AIP Advances*, *10*(3).3. Riley, F. L. (2000). Silicon nitride and related materials. *Journal of the American Ceramic Society*, *83*(2), 245-265.

4. Wen, T. (2012). *Fabrication of zinc nitride thin films using RF magnetron sputtering deposition for optoelectronic applications*. The University of Toledo.

5. Trapalis, A. (2018). *Development of Zinc Nitride Materials for Semiconductor Applications* (Doctoral dissertation, University of Sheffield).

6. Nunez, C. G., Pau, J. L., Hernandez, M. J., Cervera, M., Ruiz, E., & Piqueras, J. (2012). On the zinc nitride properties and the unintentional incorporation of oxygen. *Thin solid films*, *520*(6), 1924-1929.

7. Toyoura, K., Tsujimura, H., Goto, T., Hachiya, K., Hagiwara, R., & Ito, Y. (2005). Optical properties of zinc nitride formed by molten salt electrochemical process. *Thin Solid Films*, *492*(1-2), 88-92.7. Morosanu, C. E. (1980). The preparation, characterization and applications of silicon nitride thin films. *Thin Solid Films*, *65*(2), 171-208.

8. Ebru, Ş. T., Hamide, K., & Ramazan, E. (2007). Structural and optical properties of zinc nitride films prepared by pulsed filtered cathodic vacuum arc deposition. *Chinese Physics Letters*, *24*(12), 3477.

9. Yoo, S. H., Walsh, A., Scanlon, D. O., & Soon, A. (2014). Electronic structure and band alignment of zinc nitride, Zn 3 N 2. *Rsc Advances*, *4*(7), 3306-3311.

10. Jiang, N., Roehl, J. L., Khare, S. V., Georgiev, D. G., & Jayatissa, A. H. (2014). An ab initio computational study of pure Zn3N2 and its native point defects and dopants Cu, Ag and Au. *Thin Solid Films*, *564*, 331-338.

11. Ohring, M., Zarrabian, S., & Grogan, A. (1992). The materials science of thin films. *Appl. Opt*, *31*(34), 7162.

12. Grove, W. R. (1852). VII. On the electro-chemical polarity of gases. *Philosophical Transactions of the Royal Society of London*, (142), 87-101.

13. Ghazal, H., & Sohail, N. (2022). Sputtering Deposition. In *Thin Film Deposition-Fundamentals, Processes, and Applications*. IntechOpen.

14. Behera, A., Aich, S., & Theivasanthi, T. (2022). Magnetron sputtering for development of nanostructured materials. In *Design, Fabrication, and Characterization of Multifunctional Nanomaterials* (pp. 177-199). Elsevier.

15. Thomas, J. M. (2012). The birth of X-ray crystallography. *Nature*, *491*(7423), 186-187.

16. Tom, J. (2021, June 30). *UV-vis spectroscopy: Principle, strengths and limitations and applications*. Analysis & Separations from Technology Networks. https://www.technologynetworks.com/analysis/articles/uv-vis-spectroscopy-principle-strengths-and-limitations-and-applications-349865

17. Philips'Gloeilampenfabrieken, O. (1958). A method of measuring specific resistivity and Hall effect of discs of arbitrary shape. *Philips Res. Rep*, *13*(1), 1-9.

18. Halliday, D., Resnick, R., & Walker, J. (2013). *Fundamentals of physics*. John Wiley & Sons.

19. Jae-Sang, B. A. E. K., & Youn, J. (2006). COOLING EFFECT ENHANCEMENT IN MAGNETRON SPUTTERING SYSTEM. *continuity*, *1*, 0.

20. Xrd for Si (100)? | Researchgate. (n.d.). https://www.researchgate.net/post/XRD_for_Si_100

21. Swanepoel, R. (1983). Determination of the thickness and optical constants of amorphous silicon. *Journal of Physics E: Scientific Instruments*, *16*(12), 1214.

22. Condurache-Bota, S., Tigau, N., & Drasovean, R. (2010). Explicit application of Swanepoel's method for the analysis of Sb2O3 films. *J. Sci. Arts*, *2*(13), 335-340.